Investigating the ranges of (meta)stable phase formation in $(In_xGa_{1-x})_2O_3$: Impact of the cation coordination

C. Wouters [1], C. Sutton,[2] L. M. Ghiringhelli,[2] T. Markurt,[1] R. Schewski [1], A. Hassa [3], H. von Wenckstern,[3] M. Grundmann [3], M. Scheffler,[2] and M. Albrecht [1]

[1]*Leibniz-Institut für Kristallzüchtung, Max-Born-Straße 2, 12489 Berlin, Germany*
[2]*Fritz Haber Institute of the Max Planck Society, Faradayweg 4, 14195 Berlin, Germany*
[3]*Felix Bloch Institute for Solid State Physics, University of Leipzig, Linnéstraße 5, 04103 Leipzig, Germany*

We investigate the phase diagram of the heterostructural solid solution $(In_xGa_{1-x})_2O_3$ both computationally, by combining cluster expansion and density functional theory, and experimentally, by means of transmission electron microscopy (TEM) measurements of pulsed laser deposited (PLD) heteroepitaxial thin films. The shapes of the Gibbs free energy curves for the monoclinic, hexagonal, and cubic bixbyite alloy as a function of composition can be explained in terms of the preferred cation coordination environments of indium and gallium. We show by atomically resolved scanning TEM that the strong preference of indium for sixfold coordination results in ordered monoclinic and hexagonal lattices. This ordering impacts the configurational entropy in the solid solution and thereby the $(In_xGa_{1-x})_2O_3$ phase diagram. The resulting phase diagram is characterized by very limited solubilities of gallium and indium in the monoclinic, hexagonal, and cubic ground state phases, respectively, but exhibits wide metastable ranges at realistic growth temperatures. On the indium rich side of the phase diagram a wide miscibility gap up to temperatures higher than 1400 K is found, which results in phase separated layers. The experimentally observed indium solubilities in the PLD samples are in the range of $x = 0.45$ and $x = 0.55$ for monoclinic and hexagonal single-phase films, while for phase separated films we find $x = 0.5$ for the monoclinic phase, $x = 0.65$–0.7 for the hexagonal phase and $x \geqslant 0.9$ for the cubic phase. These values are consistent with the computed metastable ranges for each phase.

I. INTRODUCTION

Solid-solutions of group-III sesquioxides (Al_2O_3, Ga_2O_3, and In_2O_3) show promise in designing new transparent *n*-type electrodes or active materials for optoelectronic applications because of the ability to tune the bandgap energies over large ranges (i.e., 3.6–7.5 eV) by varying the relative cation concentration [1–7]. Moreover, heterostructural solid solutions such as the group-III sesquioxides where the binary components differ in their ground-state structures, offer the possibility of controlling the crystal structure by tuning the composition. This provides an additional degree of freedom for materials design beyond the effects of chemical substitution. Indeed, several current technologies such as optoelectronics [8], water splitting [9] and piezoelectronics [8,10] use structural modification by alloying as a route to widen potential applications.

To achieve the synthesis of high-quality $(In_xGa_{1-x})_2O_3$ alloys, an understanding of the phase formation as a function of composition is required. This is not a straightforward task, as Ga_2O_3 adopts a monoclinic (β) structure with space group $C2/m$ with mixed four- and sixfold cation coordination [11], while In_2O_3 has a cubic bixbyite (c) structure with space group $Ia\bar{3}$ and only sixfold cation coordination [12]. Additionally, these compounds display a rich phase space, with several polymorphs existing for both Ga_2O_3 [13,14] and In_2O_3 [15–18] that are somewhat higher in energy than

the ground-state structures. In Ga_2O_3, the α ($R\bar{3}c$) [19,20], γ ($Fd\bar{3}m$) [20,21], and orthorhombic κ ($Pna2_1$) [20,22] (in literature also sometimes referred to as ε phase) phases have all been reported in addition to the thermodynamically stable monoclinic β phase. In addition to the polymorphs of the binary compounds, a hexagonal (h) $InGaO_3$ alloy phase (see Fig. 1) with space group $P6_3mmc$ has been observed experimentally [23]. The structure contains fivefold and sixfold coordinated sites for the cations in equal amounts and is the first polymorph to accommodate Ga^{3+} in fivefold coordination. Theoretical work by Maccioni *et al.* [24] showed the remarkable stability of the h phase for $x = 0.5$. Therefore, a key question becomes: what are the ranges of stability for the different phases upon alloying in the $(In_xGa_{1-x})_2O_3$ system?

There exist two recent theoretical works on $(In_xGa_{1-x})_2O_3$, based on density functional theory (DFT) calculations with limited configurational sampling, whose results are not consistent with each other. According to Peelaers *et al.* [25], a lower bound temperature for the full miscibility of the monoclinic phase is $T = 812$ K, while Maccioni *et al.* [24] predict narrow stable ranges of $x \leqslant 0.18$ for monoclinic, $0.4 \leqslant x \leqslant 0.6$ for hexagonal and $x \geqslant 0.9$ for cubic compounds around $T = 800$ K. These works are not consistent with experimentally observed indium solubilities. Most experimental work is done on the epitaxial growth of β-$(In_xGa_{1-x})_2O_3$ thin films,
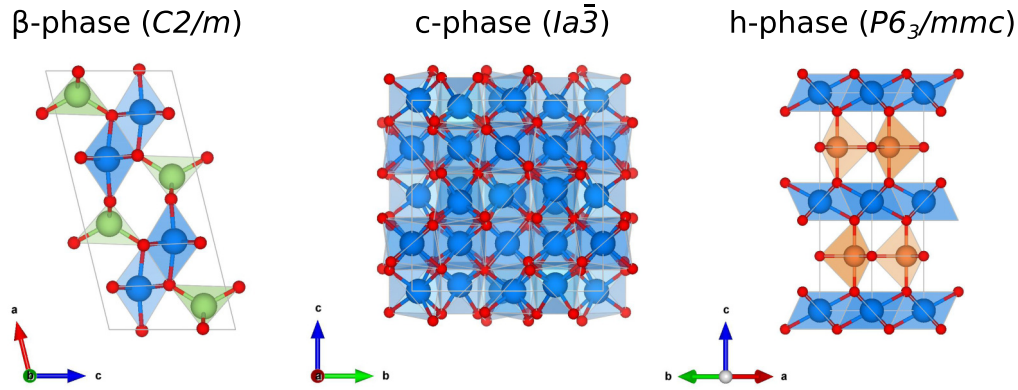
FIG. 1. The lattice symmetries for the three sesquioxides considered in this work. The monoclinic, cubic bixbyite, and hexagonal phases (referred to as β, c, and h phase in here) have mixed four-/sixfold (green/blue), only sixfold, and mixed five- (orange)/sixfold coordinated cation positions with oxygen, respectively. Made with VESTA [30].

and different indium solubility limits with different growth methods are found: $x < 0.4$ by sol-gel [5], $x = 0.04$ by metalorganic vapor phase epitaxy [26], $x = 0.15$–0.3 by pulsed laser deposition depending on substrate and growth conditions [27,28] and $x = 0.35$ by molecular beam epitaxy [4]. The work by Holder *et al.* [29] illustrated the possibility for huge metastable composition ranges in heterostructural alloys, which is something that also has to be considered for the $(\text{In}_x\text{Ga}_{1-x})_2\text{O}_3$ system, since so many polymorphs exist.

To further explore this materials system, we will reevaluate the composition and temperature dependent phase diagram of $(\text{In}_x\text{Ga}_{1-x})_2\text{O}_3$ heterostructural alloys through a joint computational and experimental investigation approach. In contrary to the existing theory studies, we employ a computationally efficient protocol to search the vast configurational space of substitutional alloys using first-principles based cluster expansion models (CE) to understand the thermodynamics of these crystalline mixtures. We compare the computed thermodynamic phase diagram with experimental results from thin $(\text{In}_x\text{Ga}_{1-x})_2\text{O}_3$ films with lateral variation of the alloy composition grown by pulsed laser deposition (PLD) that are analyzed by high-resolution transmission electron microscopy to resolve the phase formation on atomic scale. We find that the mixing enthalpy as a function of composition for the monoclinic and hexagonal phases is strongly governed by the preferred coordination environments of gallium and indium atoms and ordered structures are energetically favored. This leads to a different behavior of the configurational entropy for these phases, in contrast to the cubic bixbyite phase which can be treated as an ideal solid solution. The resulting phase diagram exhibits large metastable composition ranges that agree well with the experimentally obtained solubility limits.

II. METHODOLOGY

Experiment. The samples investigated in this work are grown on (0001)-sapphire substrates using PLD according to the continuous composition spread method [31]. In this approach, a twofold segmented $(\text{In}_2\text{O}_3)/(\text{Ga}_2\text{O}_3)$ ceramic target is rotating synchronously with the substrate, which results in a thin $(\text{In}_x\text{Ga}_{1-x})_2\text{O}_3$ film with a lateral continuously increasing average indium content. Energy dispersive x-ray spectroscopy

(EDXS) and x-ray diffraction (XRD) 2ω-θ scans are performed along the compositional gradient of the samples to retrieve the indium content as a function of the position and the spatially resolved crystallographic properties at various indium concentrations. More details on these measurements and the PLD growth technique can be found in Refs. [28,31]. Transmission electron microscopy (TEM) samples are prepared in cross-sectional view along the $\langle 1\bar{1}00 \rangle$ and $\langle 11\bar{2}0 \rangle$ lattice directions of the sapphire substrate. Conventional and scanning TEM (STEM) measurements are performed with an aberration corrected FEI Titan 80–300 electron microscope operating at 300 kV, equipped with a high-angle annular dark-field detector (HAADF). Quantification of the indium concentration in the TEM samples is carried out by measuring the indium Lα and gallium Kα peak intensities using EDXS in STEM mode and analyzed using the Cliff-Lorimer method [32]. For the STEM-EDXS measurements, a JEOL JEM2200FS TEM with acceleration voltage of 200 kV is employed.

In the experimental results, we will distinguish between the global indium content $\tilde{x}$ as determined by SEM-EDXS in the scanning electron microscope and the local indium content x as determined by STEM-EDXS in the scanning transmission electron microscope. The SEM-EDXS is performed planarly and averages over μm-sized areas of the film. Therefore, possible local variations in indium content due to nanoscale phase separation are not registered in the measurement of the global indium content $\tilde{x}$. Determination of the local indium content x is carried out in cross-section on the film by STEM-EDXS with nanoscale resolution, and will be important to determine the limits of indium/gallium incorporation in the separated phases.

Computation. The Gibbs free energy of mixing is given by

$$\Delta G_l(x, T) = \Delta H_l - T \Delta S_l, \qquad (1)$$

which is calculated for each ternary compound for each lattice type l. Here, ΔH_l is the mixing enthalpy at 0 K computed according to the equation

$$\Delta H_l = E[(\text{In}_x\text{Ga}_{1-x})_2\text{O}_3]_l - xE[\text{In}_2\text{O}_3]_c$$
$$- (1 - x)E[\text{Ga}_2\text{O}_3]_\beta, \qquad (2)$$

where $E[In_2O_3]_c$, $E[Ga_2O_3]_\beta$ and $E[(In_xGa_{1-x})_2O_3)]_l$ are the total energies per cation of the cubic (c) and monoclinic (β) binary systems and the mixed system in phase l, calculated by DFT. This definition gives an estimate of the energy relative to the stable binary phases. To calculate $E[(In_xGa_{1-x})_2O_3)]_l$, first the cluster expansion (CE) method [33–35] is applied as a numerically efficient approach to compare the energies of various lattice configurations at each composition, i.e., for different distributions of gallium and indium on the different lattice sites. The lowest energy structures at each composition and for all lattice types are then identified and their energies are recomputed using DFT and are used in Eq. (2) to obtain the mixing enthalpies at 0 K. The β, c, and h phase (see Fig. 1 for a depiction of the respective unit cells), were found to be the lowest energy phases, and thus are only considered in this work. The DFT calculations were carried out using FHI-aims [36], an all-electron full potential electronic structure code with numeric atom-centered basis functions. Tight numerical settings were used and a k-grid density of 3 k-points/Å was set using the ASE package [37] based on the convergence of the total energy. We compared two generalized gradient approximation functionals [Perdew-Burke-Ernzerhof (PBE)sol and PBE] and selected PBEsol for this study because it gives the best accuracy for predicting lattice parameters in the group-III oxide systems. The average absolute difference between the volume (normalized by the number of cations) of the DFT-optimized structures and the inorganic crystal structure database (ICSD) [38] reported structures (cards #34243, #27431, #187791, #425685, and #187792) of five experimentally reported Ga_2O_3 and In_2O_3 polymorphs is a factor of 3 lower for PBEsol compared to PBE. The PBEsol calculations are performed using a consistent 80-atom unit cell: $1 \times 1 \times 1$ (i.e., the conventional unit cell), $2 \times 2 \times 1$, and $2 \times 2 \times 2$ supercell for the c, β, and h phase, respectively. The relaxed lattice volumes increase linearly with In concentration for all lattices, as shown in the Supplemental Material [39].

The entropy term ΔS_l in Eq. (1) consists of a configurational and vibrational contribution. The configurational entropy $\Delta S_{config,l}$ is calculated using the equation for the entropy of mixing of an ideal mixture

$$\Delta S_{config,l} = -N_l k_B (x \ln x + (1-x) \ln(1-x)), \quad (3)$$

where N_l is the number of sites available for mixing in lattice type l and k_B is the Boltzmann constant. As discussed below in more detail, N_l is taken to be the number of cation sites for the cubic phase, whereas N_l is taken to be the number of coordination-specific cation sites for the monoclinic and hexagonal phases. To calculate the vibrational entropy ΔS_{vib} (independent of the lattice type) each atom (total N) is considered as a single-Debye-frequency oscillator and the mixture's Debye temperature $\Theta(x)$ is interpolated between those of the binary compounds, which are $\sim$730 K for Ga_2O_3 [40,41] and $\sim$700 K for In_2O_3 [42]. In that case, we can apply [43]

$$\Delta S_{vib} = 3N k_B((1+n) \ln(1+n) - n \ln n),$$

where $n(x, T) = [\exp(\frac{\Theta(x)}{T}) - 1]^{-1}$ is Planck's distribution. All quantities will be normalized to the number of cations.

The convex hull analysis of the free energies as a function of composition used for determination of the temperature de-

pendent phase diagram is performed using the qhull algorithm [44] in Python.

III. RESULTS

A. Experimental

We have experimentally examined a set of $(In_xGa_{1-x})_2O_3$ TEM samples with different indium concentrations that were grown by the continuous composition spread method using PLD at growth temperatures of $T_g = 913$–953 K and a background oxygen pressure of $p(O_2) = 3 \times 10^{-4}$ mbar in the PLD chamber. These samples cover the compositional range $\tilde{x} = 0.0$–0.9. TEM analysis of samples grown at $T_g = 953$ K with $\tilde{x} = 0.1$, 0.25, and 0.45 indicates that the β phase is stable at these concentrations and the layers are single phase. As an example, TEM images of the sample with $\tilde{x} = 0.45$, i.e., $(In_{0.45}Ga_{0.55})_2O_3$, are shown in Fig. 2(a), where the β phase can be identified from both electron diffraction patterns and from the atomic pattern observed in STEM-HAADF images [Fig. 2(a) bottom]. The film is not single crystalline but nanometer-sized grains of the β phase are formed, which are 60° rotated in-plane due to the hexagonal symmetry of the sapphire substrate. This explains the grainy contrast in the layer in the bright field image. The four different in-plane orientations of the monoclinic grains ([010], [0$\bar{1}$0], [132], and [1$\bar{3}$2]) are identified in the diffraction pattern. These results are consistent with the previous conclusions by von Wenckstern *et al.* [28] drawn from XRD data of the same film, which indicated that the β phase forms the major component over a composition of $0 \leqslant \tilde{x} \leqslant 0.5$.

For a higher indium concentration of $\tilde{x} = 0.55$, a single-phase hexagonal $(In_xGa_{1-x})_2O_3$ layer grown at $T_g = 913$ K was observed in TEM, as illustrated in Fig. 2(b). The diffraction pattern shows the epitaxial in-plane relationship $[1\bar{1}00]_h \parallel [11\bar{2}0]_{sapph}$ between the hexagonal phase of the layer and the corundum sapphire substrate. In these samples, the layer is not single crystalline but the hexagonal phase consists of different grains with slight off-orientations with respect to each other. This is obvious from the diffuse diffraction spots and explains the short-range contrast variations in the bright field image. On the STEM image in the [11$\bar{2}$0] orientation, some stacking faults can be observed indicating a defective hexagonal structure.

For even higher indium contents, phase separation is consistently observed in the PLD layers. At $T_g = 953$ K, the relative x-ray peak intensities of the different phases in Ref. [28] indicate that the h phase is the predominant phase for $0.5 < \tilde{x} \leqslant 0.7$, while the c phase is dominating for $0.7 < \tilde{x} \leqslant 1$. TEM bright field and STEM-HAADF analysis of this 953 K sample at an indium content of $\tilde{x} = 0.75$ reveals a layered structure indicative of phase separation, as shown in Fig. 3. The β phase is observed at the interface to the substrate, followed by the h phase, and the c phase forming at the surface. For this phase separated sample at $\tilde{x} = 0.75$, different local indium contents (measured using STEM-EDXS) of $x = 0.5$ for the β phase, $x = 0.65$–0.7 for the h phase, and $x \geqslant 0.9$ for the c phase are found. Similar to the single-phase layers, the β and h phase present small grains, while the cubic phase is almost single-crystalline, as apparent by the more
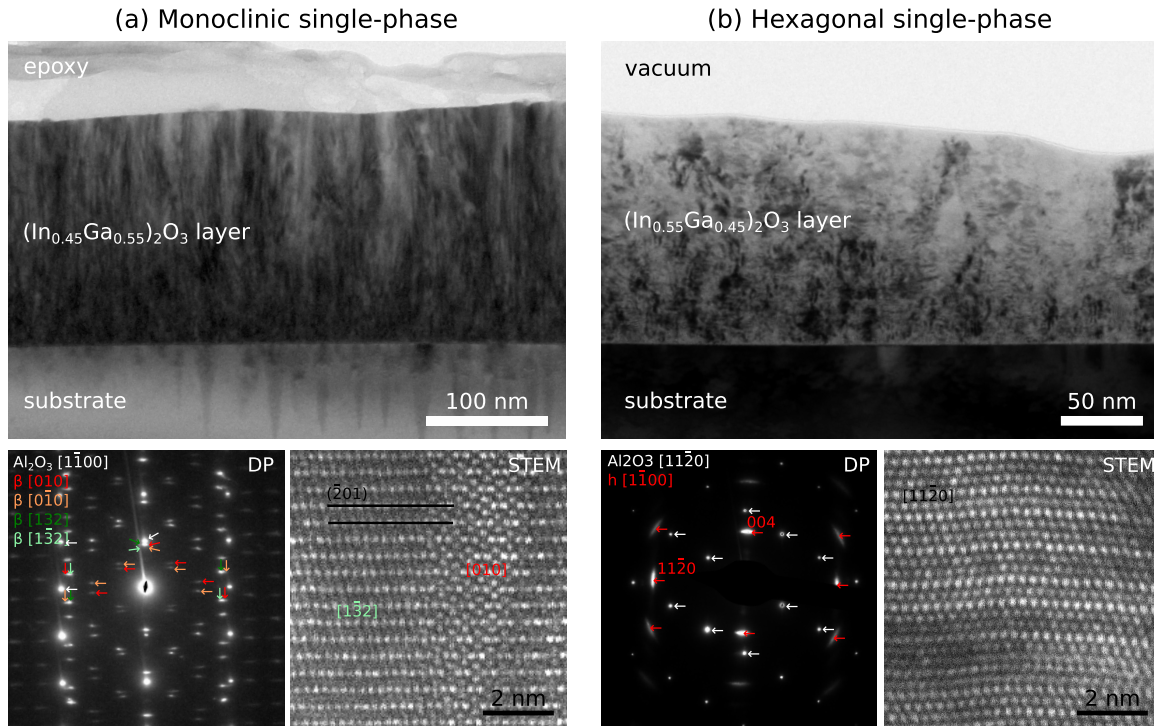
FIG. 2. TEM images of single-phase (a) monoclinic $(In_{0.45}Ga_{0.55})_2O_3$ and (b) hexagonal $(In_{0.55}Ga_{0.45})_2O_3$ thin films on sapphire grown, respectively, at $T_g = 953$ K and $T_g = 913$ K. On top are TEM bright field images showing the morphology of the layer. The bottom left on each side shows the diffraction pattern of the Al_2O_3 substrate (white arrows) and the layer (colored arrows) together. For the monoclinic film, four different in-plane orientations can be recognized. Two of them are also identified in the STEM image, which shows the atomic pattern of a [010] and a [1$\bar{3}$2] grain and their common growth along the ($\bar{2}$01) planes. The STEM image of the hexagonal phase is taken in the [11$\bar{2}$0] orientation and presents some stacking faults.

homogeneous intensity in the bright field image [Fig. 3(a)]. As a result, for the β phase and h phase, the STEM-EDXS measurement is averaged over different nm-sized grains because of the unavoidable sample drift and instabilities of the stage during the measurement. This is not an issue for the c phase because of the bigger grain sizes.

The same types of STEM-EXDS measurements were done for a second phase separated layer, which was grown at $T_g = 913$ K and has a global indium content of $\tilde{x} = 0.8$. For this layer, a grainy hexagonal phase was identified at the interface with a local indium content of $x \approx 0.7$. On top of that layer, a cubic $(In_xGa_{1-x})_2O_3$ phase was found with a local indium content of $x \approx 0.9$. Contrary to the other phase separated sample, in this layer no monoclinic phase was found in the TEM measurements.

High-resolution STEM-HAADF (STEM Z contrast) imaging in the TEM is used to determine the lattice site occupations of the gallium and indium atoms in the β-, h-, and c-$(In_xGa_{1-x})_2O_3$ alloys (Fig. 4). The respective indium contents for the images presented in Fig. 4 are $x = 0.45, 0.55$, and 0.9. Performing STEM-HAADF along a high symmetry zone-axis direction of the crystal provides information about the composition of atomic columns as their intensity scales roughly as Z^2 (Rutherford scattering), where Z is the average atomic number along the atomic column. This means that a higher intensity is observed when heavier indium atoms are present in a column. By imaging in the [010] ([11$\bar{2}$0]) orienta-

tions of the β (h) phase, the well-ordered columns consist solely of four- (five)fold or sixfold coordinated cations. Individual four/five/sixfold coordinated cation columns in the STEM-HAADF images have been identified by comparing the high-resolution image pattern to stick-and-ball models of the respective phases (see insets in Fig. 4). The black intensity line profiles shown at the bottom are averages of multiple line scans extracted along two differently coordinated cation columns for the β and h phase. The higher STEM-HAADF intensity on the sixfold lattice positions (octahedral, blue ball in Fig. 4) compared to the four- and fivefold lattice sites for the β and h phase, respectively, indicates in both cases a preference of indium for the sixfold coordination environment. To quantify this, we added the red intensity line profiles for simulated STEM-HAADF images of ordered monoclinic and hexagonal lattices with $x = 0.45$ and $x = 0.55$, respectively. In the monoclinic simulated structure, all indium atoms are randomly distributed on octahedral sites only; in the hexagonal simulated structure, all octahedral sites are occupied by indium and the remaining 5% of indium is randomly distributed on the tetrahedral sites. For the hexagonal phase we find a perfect agreement between experiment and simulation, while for the monoclinic phase the trend is similar but the intensity difference is slightly higher for the experimental structure. A possible explanation for this small discrepancy could be a locally higher indium content with all extra indium atoms on the octahedral sites as well.
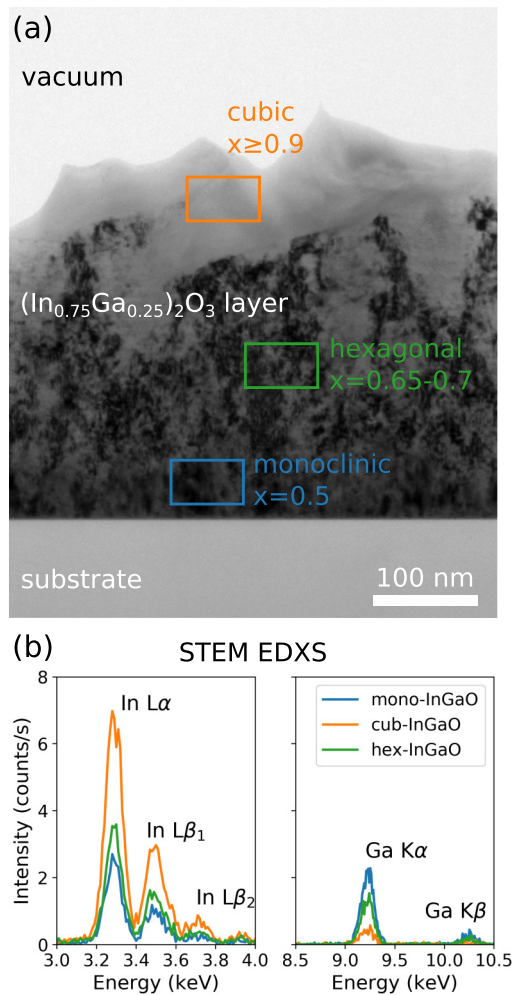
FIG. 3. (a) TEM bright field image of a phase separated $(In_{0.75}Ga_{0.25})_2O_3$ thin film on sapphire substrate grown at $T_g = 953$ K. The local indium content x in the monoclinic, hexagonal, and cubic regions is determined by the STEM-EDXS measurement shown in (b).

In contrast, all cation lattice sites have the same sixfold environment in c-$(In_xGa_{1-x})_2O_3$, and therefore, only slight variations in the intensity are observed in the STEM-HAADF images due to the statistical incorporation of the gallium atoms. These results indicate that the occupation of the lattice sites by indium and gallium is consistent between the various phases across all examined compositions. These results provide experimental evidence for the strong energetic preference of In^{3+} for an octahedral coordination environment.

B. Computation

To understand the topology of the phase diagram, we start with a discussion of the PBEsol-computed ΔH values (in eV/cation) of the lowest-energy structures at $T = 0$ K over the composition range $x = 0 - 1$ identified by CE [see Fig. 5(a)]. ΔH for the c phase displays a concave parabolic shape over the whole composition range with a maximum close to $x = 0.5$ because of the presence of only one sixfold coordinated cation site in this phase. Indeed,

this energy surface is reminiscent of the classical energy of mixing with increasing concentration for an alloy with only one lattice site, e.g., $(In_xGa_{1-x})N$ in the wurtzite structure [29,45]. In contrast, the evolution of ΔH for the β and h phases differs qualitatively from the classical behavior of the c phase because these structures contain mixed four-/sixfold and mixed five-/sixfold coordinated cation sites with oxygen, respectively. For both phases, the lowest energy structures in the range $0 < x \leqslant 0.5$ correspond to those where indium is incorporated only into the sixfold coordinated lattice sites. For the β phase, this results in a flat evolution in the mixing enthalpy with an increasing indium concentration, reaching a local maximum of $\Delta H = 0.035$ eV/cation around $x = 0.34$ that decreases to $\Delta H = 0.024$ eV/cation at $x = 0.5$. At this concentration, all gallium atoms occupy the fourfold coordinated positions, and all indium atoms occupy the sixfold positions, creating a long-range ordered structure where all indium and gallium atoms are in their preferred coordination environment. The h phase is very unstable for $x = 0$ ($\Delta H = 0.167$ eV/cation) and $x = 1$ ($\Delta H = 0.23$ eV/cation) but displays a concave energy evolution and reaches a minimum at $x = 0.5$ ($\Delta H = -0.008$ eV/cation). At this concentration, the lowest-energy structure corresponds to one with all gallium atoms on the fivefold sites and all indium atoms on the sixfold sites. Because of the equal amounts of sixfold/fourfold and sixfold/fivefold coordinated cation sites in the β and h phase, respectively, indium atoms for alloys with $x > 0.5$ can only be incorporated into the fourfold/fivefold coordinated cation sites, which is energetically destabilizing and leads to the observed steep increase in energy for $x > 0.5$. The discontinuity in the monoclinic ΔH curve around $x = 0.9$ is a result of the FHI-aims optimization, which does not enforce a global symmetry during the geometry optimization [46]. The unconstrained relaxation effectively allows the system to break its symmetry and to descend into a lower energy structure, which results in a strongly deformed lattice for the unstable monoclinic phase at high In concentrations. Because these high-energy states do not play a determining role in the construction of the phase diagram, this result does not affect the interpretation of the results. The ΔH data points are fitted to a single parabola for the cubic phase and two distinct parabolas for $x \leqslant 0.5$ and $x > 0.5$ for the β and h phase to reproduce the sharp edges at $x = 0.5$. The fitted curves will be used for the calculations of ΔG.

The large influence of the specific occupation site of gallium and indium on ΔH is highlighted in Fig. 6, where mixing enthalpies are calculated for about 100 random configurations of all three lattice structures at $x = 0.5$. The mean effective coordination number (ECN) [47] of indium and gallium is determined for each configuration and plotted as a function of ΔH. Clear trends can be observed for the β and h phase of respective decreasing and increasing ECN for indium and gallium with increasing mixing enthalpy. The lowest energy configurations in both phases are the one with all indium atoms on sixfold sites and all gallium atoms on four- or fivefold sites. Going away from these ordered structures by displacing indium and gallium atoms to the other coordination environment causes a strong increase in the mixing enthalpy. This is in strong contrast with the situation for the c phase,
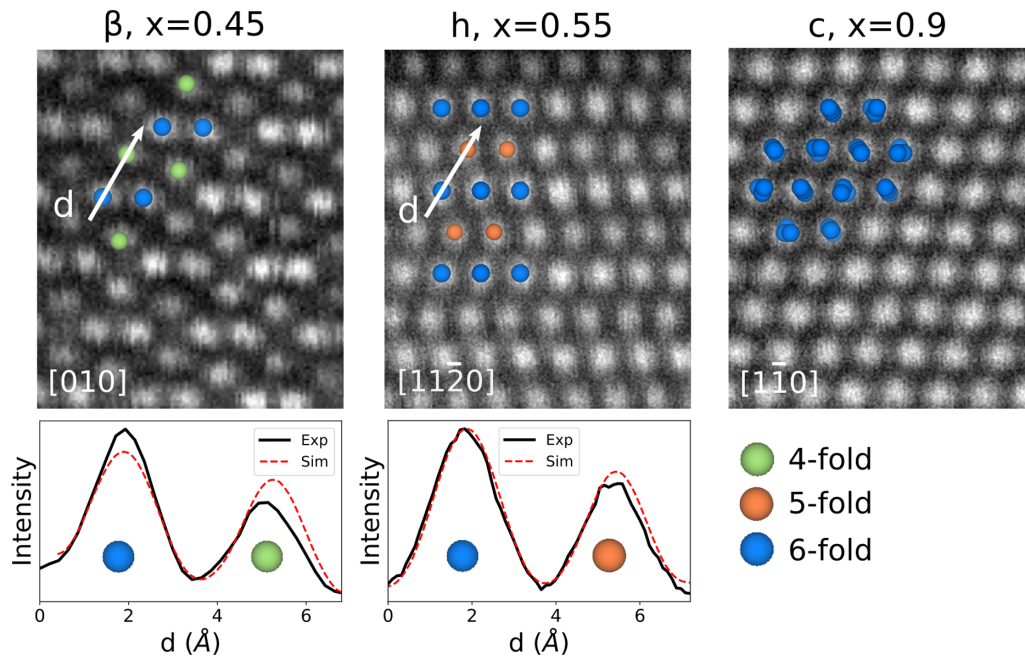
FIG. 4. Experimental high-magnification STEM-HAADF images (several images summed to enhance contrast) of the β-, h-, and c-$(In_xGa_{1-x})_2O_3$ alloys with overlay of the stick-and-ball models without oxygen atoms. The lower plots show experimental HAADF intensity line profiles (black, multiple averaged) from the STEM images along the two differently coordinated atom columns in the β and h lattices, compared to the simulated profiles (red) for ordered structures. The intensity difference between the four-/fivefold and sixfold atomic columns, respectively, proves the preferential incorporation of the heavier indium to the sixfold lattice sites.

where the spread on the mixing enthalpies is very small since there is only one type of coordination site. This result explains the ordered β and h structures that we have observed in the STEM images in Fig. 4, where indium is sitting mostly on the octahedral lattice sites.

The configurational entropy is calculated according to the ideal solution model which assumes a random distribution of the two components on the cation sites [Eq. (3)]. However, we note a different value of N_l is used to account for a difference in the cation site degeneracy in the c phase compared with the β and h phase. When N_l is taken to be the number of cations, this results in the orange curve in Fig. 5(b). This is used for the cubic phase because the unit cell only contains six-coordinate cation sites, which will lead to indium and gallium mixing on all sites with equal probability. However, based on the results of Fig. 6 and the experimental results showing a strong preference of indium for the sixfold sites, mixing is not ideal in the monoclinic and hexagonal phase. Instead, we assume that for $x < 0.5$ indium is only mixing on the sixfold sites, for $x = 0.5$ β and h structures are highly ordered, and for $x > 0.5$ indium is mixing only on four-/fivefold sites in β-/h-$(In_xGa_{1-x})_2O_3$, respectively. This means that the entropy is zero at $x = 0.5$, and that $N_l \rightarrow 1/2N_l$ and $x \rightarrow 2x$ for $x < 0.5$ and $x \rightarrow 2(1-x)$ for $x > 0.5$ in Eq. (3), which gives the blue curve for the entropy in Fig. 5(b). A more detailed justification for the different treatments of the configurational entropy for the different phases is given in the Supplemental Material [39]. The vibrational entropy, which ranges in between 10^{-7}–10^{-9} eV/cation depending on T and x, is negligible compared to the configurational entropy and therefore not added to the plot.

Using the total entropy, the Gibbs free energies are calculated as a function of indium content for each phase for various temperatures. The free energy curves are plotted for $T = 600$ K and $T = 1000$ K in Figs. 5(c) and 5(d). The thermodynamically stable phases and compositions can now be identified through the construction of the convex hull [48,49], which is comprised of a series of common tangent lines between the lowest free energy structures at various compositions on the free energy-composition surface. The convex hull at $T = 0$ K (i.e., without any entropic contributions) is given by the black line and crosses in Fig. 5(a), which indicates there are only three stable structures at $x = 0$ (β phase), $x = 0.5$ (h phase), and $x = 1$ (c phase). The unstable mixtures in the range $0.0 < x < 0.5$ will phase separate into β-Ga_2O_3 and h-$InGaO_3$ ($x = 0.5$). For the indium-rich regime ($0.5 < x < 1$), the negative curvature indicates phase separation into h-$InGaO_3$ ($x = 0.5$) and c-In_2O_3 ($x = 1$). At higher temperatures, the free energy curves become more convex due to the $-T\Delta S$ term, and more compositions will become stable, as can be seen for $T = 1000$ K in Fig. 5(d). The limiting compositions for stability for each phase and for temperatures up to 1400 K are plotted in Fig. 7 by the dotted lines (binodals). The blue, green, and orange filled regions then define the thermodynamic stable ranges for the β, h, and c phase, respectively. The stable range is rather narrow, especially for the h phase, which is practically only stable at $x = 0.5$ for all temperatures. The monoclinic phase is stable for a larger compositional window compared with the cubic one due to the rather flat ΔH curve for the β phase for $x \leqslant 0.5$.

Since epitaxial growth methods (e.g., like PLD) do not typically operate at thermodynamic equilibrium, it is also

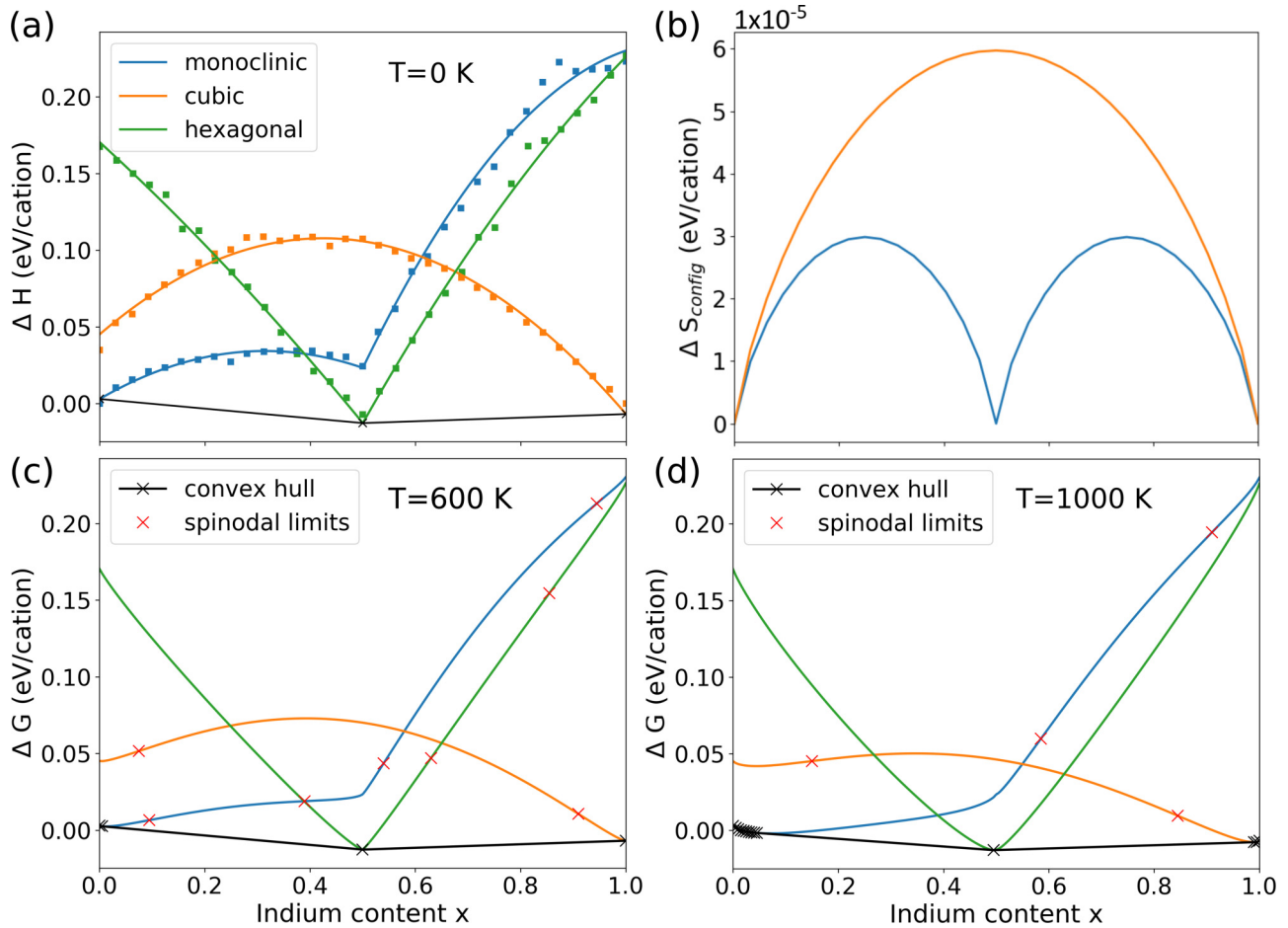FIG. 5. (a) Mixing enthalpies (ΔH) at 0 K for the lowest energy configurations of the monoclinic (β), hexagonal (h), and cubic bixbyite (c) lattices calculated by DFT using the PBEsol functional with fit lines to the data. (b) Configurational entropy (ΔS_{config}) for the three phases (green and blue curves are overlapped), calculated as described in the text. (c) and (d) Free energies (ΔG) at $T = 600$ K and $T = 1000$ K as a function of indium content for the β, h, and c phase. The global convex hull is indicated by the black crosses and line. The spinodal limits at elevated temperatures are indicated with red crosses.

interesting to define metastable ranges in the $(In_xGa_{1-x})_2O_3$ phase diagram. To do this, we follow the work of Holder *et al.* [29], who have constructed phase diagrams including metastable regions for heterostructural materials systems,
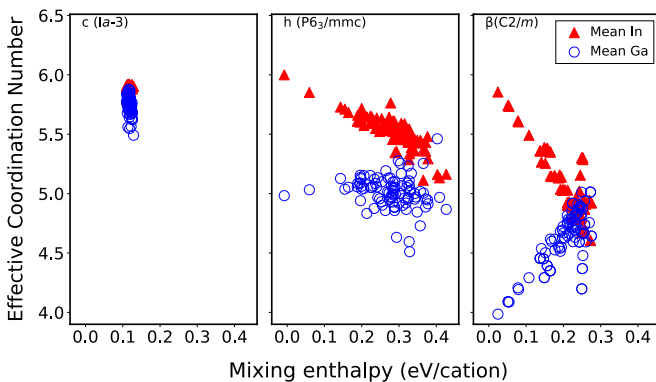

FIG. 6. Mean effective coordination number of indium and gallium and corresponding ΔH values for about 100 randomly generated structures for c-$InGaO_3$ (left), h-$InGaO_3$ (middle), and β-$InGaO_3$ (right), i.e., $x = 0.5$.

like MgZnO. Compounds are labeled as metastable, meaning stable against small composition fluctuations, when the free energy curve is convex, i.e., $d^2G/dx^2 > 0$. The zero crossings of d^2G/dx^2 at the two illustrated temperatures of 600 and 1000 K are indicated by the red crosses in Figs. 5(c) and 5(d) for each phase. These limiting compositions form the so-called spinodal in the phase diagram, plotted by the squared colored lines in Fig. 7 for each phase. Metastable compounds are then found in the region in the phase diagram between the binodal and the spinodal lines. The black lines in the phase diagram define the critical compositions for a phase transition, i.e., where the lowest energy structure changes from (1) monoclinic to hexagonal and from (2) hexagonal to cubic. They additionally limit the metastable region for each phase separately. At these critical compositions, the two touching phases have the same free energy. However, since the different phases have crystal symmetries that are related through a reconstructive transformation, bond breaking is required for the phase transition (to change the coordination environments) which imposes a high (free) energy barrier. Additionally, from Fig. S2 in the Supplemental Material [39], we can infer that a discontinuity in the
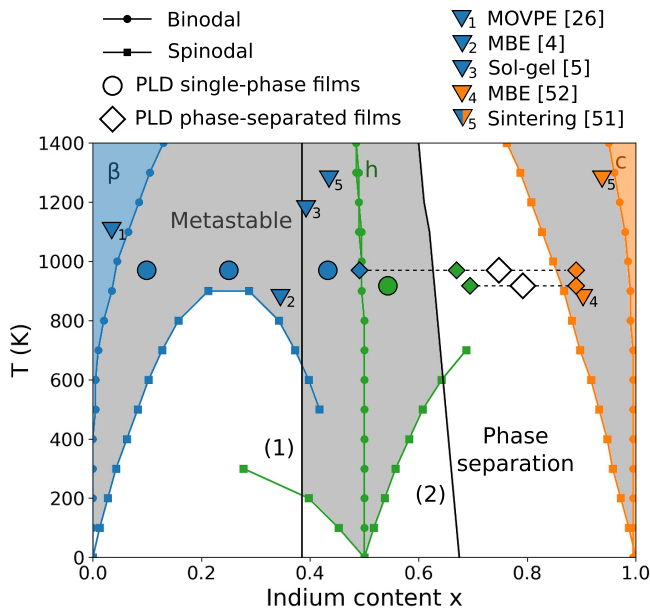
FIG. 7. Computed temperature dependent phase diagram for $(In_xGa_{1-x})_2O_3$ including binodal and spinodal lines for the monoclinic (blue), hexagonal (green), and cubic (orange) phases. Thermodynamic stable composition ranges are color-filled, metastable ranges are grey, and for the white area below the spinodal lines phase separation is expected. The black vertical lines indicate the critical compositions where the lowest energy phase changes from (1) monoclinic to hexagonal and from (2) hexagonal to cubic. Experimental data points from PLD layers studied in this work (circles and diamonds) and from other synthesis methods found in literature (triangles) are added as symbols. The white diamonds denote the global compositions of the phase separated films.

lattice volume, especially between the monoclinic and hexagonal phase, will occur at the critical compositions. Hence realistically, these phase transformations require an external energy input to accomplish the lattice changes.

For growth temperatures above 900 K, a large metastable region on the gallium rich side extends up to indium contents around $x = 0.6$, containing the monoclinic compound up to $x = 0.385$ and the hexagonal compound for $0.385 \leqslant x \leqslant 0.63$. For the monoclinic phase, this large metastable window is a result of the flat behavior of its ΔH curve in the range $0 \leqslant x \leqslant 0.5$ [see Fig. 5(a)]. This in turn follows from the fact the indium can be accommodated in its preferred sixfold coordinated environment for this composition range. As a result of this, for increasing temperatures, the free energy curve will relatively quickly convert to a convex shape due to the entropy contribution. While for ideal mixtures, the spinodal is concave parabolic with a maximum at $x = 0.5$ where there is maximum disorder, the monoclinic spinodal in this case presents this behavior over the range $0 \leqslant x \leqslant 0.5$ with the maximum at $x = 0.25$ where there is maximal disorder on the octahedral sites. On the indium-rich side a miscibility gap remains up to temperatures higher than 1400 K, where phase separation is expected into a hexagonal and a cubic alloy. The phase diagram obeys Gibbs phase rule for a binary system at constant pressure [50], and the reasoning for this is worked out in the Supplemental Material [39].

IV. DISCUSSION

As a comparison between the computational and experimental results, the experimentally determined compositions from single-phase (circles) and phase-separated (diamonds) PLD samples studied in this work have been overlaid on the computed phase diagram in Fig. 7. Additionally, literature data points (triangles) representing indium and gallium solubility limits, respectively, in monoclinic [4,5,26,51] and cubic [51,52] $(In_xGa_{1-x})_2O_3$ alloys grown or prepared by different methods have been added.

A first observation is that almost all experimental compositions strongly exceed the narrow calculated thermodynamic stability ranges, and actually fit better to the calculated metastable windows. This means most synthesis methods are generating metastable material. For the films grown by PLD and molecular beam epitaxy (MBE), this follows from the fact that during growth, the surface diffusion allows the atoms to locally find their preferred position and preferred coordination environment, so that the low energy but metastable ordered monoclinic and hexagonal phases can be achieved. In β-$(In_xGa_{1-x})_2O_3$ grown by metalorganic vapour phase epitaxy (MOVPE) at $T = 1100$ K [26], which is the growth method closest to thermodynamic equilibrium, the allowed indium incorporation before phase separation takes place does agree well with the predicted thermodynamic limit. For sintered $(In_xGa_{1-x})_2O_3$ powders [51] that were heated for several days to reach equilibrium, the measured Ga solubility limit in In_2O_3 fits well to our calculation of the thermodynamic limit at 1275 K, while the In solubility limit in Ga_2O_3 falls in the calculated metastable regime. We may note here that bulk diffusion in covalently bonded materials is limited and may be hampered by the high kinetic barrier to break bonds. Even for the powder sintering approach [51], it is therefore not evident that the broad stability range of the monoclinic phase, obtained after extended heating is the true thermodynamical equilibrium phase as claimed or just a metastable state as indicated by our calculations. We note additionally that all the discussed samples were not grown/prepared under the exact same oxygen regime, which is another important factor influencing the solubility limit of the occurring phases besides the temperature but is not incorporated in our calculations. This, however, does not affect the main conclusion that it is the ordering that causes the broad metastable range of compositions and thereby extends the solubility as compared to thermodynamic equilibrium, which strongly enhances application-oriented perspectives for these $(In_xGa_{1-x})_2O_3$ alloys.

At $x = 0.5$, both the β and h phase display ordered structures as the lowest energy configuration and their mixing enthalpies reach (local) minima. Of the two, the hexagonal phase is slightly lower in energy and therefore the expected phase with a metastability range of approximately $0.385 \leqslant x \leqslant 0.63$ at realistic growth temperatures. Experimentally however, both phases are observed close to this composition range. The calculated energy difference between the β and the h phase in this critical region around $x = 0.5$ is 32 meV/cation ($=12.8$ meV/atom), which is on the order of the DFT accuracy found for similar oxide systems (24 meV/atom from Ref. [53]). Therefore, we could argue that both metastable

phases are competing close to $x = 0.5$ and both can be achieved.

The computed miscibility gap on the indium rich side stays up to temperatures above 1400 K, because the ΔH curves of the h and c phase are much steeper there. The miscibility gap is well reproduced in experiment, as samples with global compositions of $\tilde{x} = 0.75$ and $\tilde{x} = 0.80$, and grown, respectively, at $T = 953\,\mathrm{K}$ and $T = 913\,\mathrm{K}$, indeed present phase separation. In this temperature range, the separated metastable phases according to calculation would be the h phase with $x \approx 0.63$ and the c phase with $x \approx 0.86$. This computed indium composition of the cubic phase agrees very well with the experimental compositions, both for our PLD layers and the reported MBE layer [52]. The computed indium limit of $x = 0.63$ for the hexagonal phase is exceeded in our PLD layers, where we get a maximum incorporation of $x = 0.7$. This could possibly be explained by the defective structure of the hexagonal phase in experimental films, which could allow for more indium to be incorporated.

V. CONCLUSION

In contrast to standard models of mixing, we have shown that interesting phases of heterostructural $(\mathrm{In}_x\mathrm{Ga}_{1-x})_2\mathrm{O}_3$ alloys could be achieved, because the different preferred coordination environments of the component elements are satisfied. The accommodation of indium in the preferred sixfold environment leads to low mixing enthalpies in the composition range $0 \leqslant x \leqslant 0.5$ for β-$(\mathrm{In}_x\mathrm{Ga}_{1-x})_2\mathrm{O}_3$ and a remarkable

stability for h-$(\mathrm{In}_x\mathrm{Ga}_{1-x})_2\mathrm{O}_3$ close to $x = 0.5$. This leads to large metastable windows in the gallium rich regime of the phase diagram for both phases. Indeed, it is experimentally confirmed that a large composition range of the monoclinic alloy can be grown ($x \leqslant 0.5$) as well as the hexagonal alloy at intermediate compositions up to $x = 0.7$. On the indium rich side of the phase diagram, a miscibility gap remains up to high temperatures, which is confirmed in the experimental films which display phase separation. The c phase, which has only one type of coordination site, is stable for $x \geqslant 0.9$ for growth temperatures around $T = 1000\,\mathrm{K}$, which fits well to the predicted metastable limit.

[1] F. Yang, J. Ma, C. Luan, and L. Kong, Appl. Surf. Sci. **255**, 4401 (2009).

[2] L. Kong, J. Ma, F. Yang, C. Luan, and Z. Zhu, J. Alloys Compd. **499**, 75 (2010).

[3] L. Kong, J. Ma, C. Luan, and Z. Zhu, J. Solid State Chem. **184**, 1946 (2011).

[4] T. Oshima and S. Fujita, Phys. Status Solidi C **5**, 3113 (2008).

[5] Y. Kokubun, T. Abe, and S. Nakagomi, Phys. Status Solidi Appl. Mater. Sci. **207**, 1741 (2010).

[6] F. Zhang, K. Saito, T. Tanaka, M. Nishio, and Q. Guo, Solid State Commun. **186**, 28 (2014).

[7] H. Ito, K. Kaneko, and S. Fujita, Jpn. J. Appl. Phys. **51**, 09LD16 (2012).

[8] J. Vidal, S. Lany, J. Francis, R. Kokenyesi, and J. Tate, J. Appl. Phys. **115**, 113507 (2014).

[9] H. Peng, P. F. Ndione, D. S. Ginley, A. Zakutayev, and S. Lany, Phys. Rev. X **5**, 021016 (2015).

[10] Y. Saito, H. Takao, T. Tani, T. Nonoyama, K. Takatori, T. Homma, T. Nagaya, and M. Nakamura, Nature (London) **432**, 84 (2004).

[11] S. Geller, J. Chem. Phys. **33**, 676 (1960).

[12] M. Marezio, Acta Crystallogr. **20**, 723 (1966).

[13] R. Roy, V. G. Hill, and E. F. Osborn, J. Amer. Chem. Soc. **74**, 719 (1952).

[14] H. Y. Playford, A. C. Hannon, E. R. Barney, and R. I. Walton, Chem. Eur. J. **19**, 2803 (2013).

[15] D. Liu, W. W. Lei, B. Zou, S. D. Yu, J. Hao, K. Wang, B. B. Liu, Q. L. Cui, and G. T. Zou, J. Appl. Phys. **104**, 083506 (2008).

[16] M. Epifani and P. Siciliano, J. Am. Chem. Soc. **126**, 4078 (2014).

[17] M. F. Bekheet, M. R. Schwarz, S. Lauterbach, H. J. Kleebe, P. Kroll, R. Riedel, and A. Gurlo, Angew. Chemie - Int. Ed. **52**, 6531 (2013).

[18] H. Yusa, T. Tsuchiya, J. Tsuchiya, N. Sata, and Y. Ohishi, Phys. Rev. B **78**, 092107 (2008).

[19] H. Nishinaka, D. Tahara, S. Morimoto, and M. Yoshimoto, Mater. Lett. **205**, 28 (2017).

[20] V. Gottschalch, S. Merker, S. Blaurock, M. Kneiß, U. Teschner, M. Grundmann, and H. Krautscheid, J. Cryst. Growth **510**, 76 (2019).

[21] H. Y. Playford, A. C. Hannon, M. G. Tucker, D. M. Dawson, S. E. Ashbrook, R. J. Kastiban, J. Sloan, and R. I. Walton, J. Phys. Chem. C **118**, 16188 (2014).

[22] I. Cora, F. Mezzadri, F. Boschi, M. Bosi, M. Čaplovičová, G. Calestani, I. Dódony, B. Pécz, and R. Fornari, CrystEngComm **19**, 1509 (2017).

[23] R. D. Shannon and C. T. Prewitt, J. Inorg. Nucl. Chem. **30**, 1389 (1968).

[24] M. B. Maccioni and V. Fiorentini, Appl. Phys. Express **9**, 041102 (2016).

[25] H. Peelaers, D. Steiauf, J. B. Varley, A. Janotti, and C. G. Van de Walle, Phys. Rev. B **92**, 085206 (2015).

[26] S. Bin Anooz, A. Popp, R. Grüneberg, C. Wouters, R. Schewski, M. Schmidbauer, M. Albrecht, A. Fiedler, M. Ramsteiner, D. Klimm, K. Irmscher, Z. Galazka, and G. Wagner, J. Appl. Phys. **125**, 195702 (2019).

[27] C. Kranert, M. Jenderka, J. Lenzner, M. Lorenz, H. Von Wenckstern, R. Schmidt-Grund, and M. Grundmann, J. Appl. Phys. **116**, 013505 (2014).

[28] H. Von Wenckstern, D. Splith, M. Purfürst, Z. Zhang, C. Kranert, S. Müller, M. Lorenz, and M. Grundmann, Semicond. Sci. Technol. **30**, 024005 (2015).

[29] A. M. Holder, S. Siol, P. F. Ndione, H. Peng, A. M. Deml, B. E. Matthews, L. T. Schelhas, M. F. Toney, R. G. Gordon, W. Tumas, J. D. Perkins, D. S. Ginley, B. P. Gorman, J. Tate, A. Zakutayev, and S. Lany, Sci. Adv. **3**, e1700270 (2017).

[30] K. Momma and F. Izumi, J. Appl. Crystallogr. **44**, 1272 (2011).

[31] H. Von Wenckstern, Z. Zhang, F. Schmidt, J. Lenzner, H. Hochmuth, and M. Grundmann, Cryst. Eng. Commun. **15**, 10020 (2013).

[32] G. Cliff and G. W. Lorimer, J. Microsc. **103**, 203 (1975).

[33] J. M. Sanchez, F. Ducastelle, and D. Gratias, Phys. A **128**, 334 (1984).

[34] D. De Fontaine, *Solid State Physics*, Vol. 47 (Academic, Elsevier B.V, Amsterdam, 1994).

[35] F. Ducastelle, *Order and Phase Stability in Alloys* (North-Holland, Amsterdam, 1991).

[36] V. Blum, R. Gehrke, F. Hanke, P. Havu, V. Havu, X. Ren, K. Reuter, and M. Scheffler, Comput. Phys. Commun. **180**, 2175 (2009).

[37] A. H. Larsen, J. J. Mortensen, J. Blomqvist, I. E. Castelli, R. Christensen, M. Dułak, J. Friis, M. N. Groves, B. Hammer, C. Hargus, E. D. Hermes, P. C. Jennings, P. B. Jensen, J. Kermode, J. R. Kitchin, E. L. Kolsbjerg, J. Kubal, K. Kaasbjerg, S. Lysgaard, J. B. Maronsson, T. Maxson, T. Olsen, L. Pastewka,

A. Peterson, C. Rostgaard, J. Schiøtz, O. Schütt, M. Strange, K. S. Thygesen, T. Vegge, L. Vilhelmsen, M. Walter, Z. Zeng, and K. W. Jacobsen, J. Phys. Condens. Matter **29**, 273002 (2017).

[38] G. Bergerhoff and I. D. Brown, in *Crystallogr. Databases*, edited by F. H. Allen *et al.* (International Union of Crystallography, Chester, UK, 1987).

[39] See Supplemental Material at http://link.aps.org/supplemental/10.1103/PhysRevMaterials.4.125001 for a justification of the treatment of the configurational entropy, the DFT lattice volumes as a function of indium concentration, and Gibb's phase rule applied to the presented phase diagram.

[40] M. D. Santia, N. Tandon, and J. D. Albrecht, Solid State Commun. **297**, 1 (2019).

[41] Z. Guo, A. Verma, X. Wu, F. Sun, A. Hickman, T. Masui, A. Kuramata, M. Higashiwaki, D. Jena, and T. Luo, Appl. Phys. Lett. **106**, 111909 (2015).

[42] N. Preissler, O. Bierwagen, A. T. Ramu, and J. S. Speck, Phys. Rev. B **88**, 085305 (2013).

[43] B. Fultz, Prog. Mater. Sci. **55**, 247 (2010).

[44] C. B. Barber, D. P. Dobkin, and H. Huhdanpaa, ACM Trans. Math. Softw. **22**, 469 (1996).

[45] I. H. Ho and G. B. Stringfellow, Appl. Phys. Lett. **69**, 2701 (1996).

[46] F. Knuth, C. Carbogno, V. Atalla, V. Blum, and M. Scheffler, Comput. Phys. Commun. **190**, 33 (2015).

[47] R. Hoppe, Z.Kristallogr. **150**, 23 (1979).

[48] R. B. Israel, Commun. Math. Phys. **43**, 59 (1975).

[49] A. N. Varchenko, J. Sov. Math. **52**, 3305 (1990).

[50] J. Williard Gibbs, *The Scientific Papers of J. Williard Gibbs, Vol.1*, *Thermodynamics* (Dover, New York, 1961).

[51] D. D. Edwards, P. E. Folkins, and T. O. Mason, J. Am. Ceram. Soc. **80**, 253 (1997).

[52] A. Papadogianni, T. Nagata, C. Wouters, M. Albrecht, and O. Bierwagen (unpublished).

[53] G. Hautier, S. P. Ong, A. Jain, C. J. Moore, and G. Ceder, Phys. Rev. B **85**, 155208 (2012).

[54] https://dx.doi.org/10.17172/NOMAD/2020.06.30-1.